Supplementary Information

Lignosulfonate molecular anchoring of polyaniline for high performance sodium-ion battery anodes

Yifan Tong,[a] Hao Zhuo,*[b] Shuai Zhang,[a] Haihong Lai,[a] Qi Wang,[a] Zhenhua Dai,[a] Hongzhi Zheng,[a] Xinwen Peng*[a] and Linxin Zhong*[a]

[a] State Key Laboratory of Advanced Papermaking and Paper-based Materials, South China University of Technology, Guangzhou 510641, China.

E-mail: fexwpeng@scut.edu.cn, lxzhong0611@scut.edu.cn

[b] Department of Mechanical Engineering, National University of Singapore, 9 Engineering Drive 1, Singapore 117575, Singapore.

E-mail: zhuoh14@gmail.com

Experimental Section

Materials

SL was supplied by Macklin Biochemical Co., Ltd. (Shanghai, China). Aniline (ANI), intrinsic PANI, and ammonium persulfate (APS) were purchased from Aladdin Biochemical Technology Co., Ltd. (Shanghai, China). The industrial Kraft lignin was obtained from Dongsheng New Materials (Shandong) Co., Ltd., as a waste product derived from softwood Kraft pulping. Reagents related to lignin sulfonation, including formaldehyde solution, sodium sulfite (Na_2SO_3) and sodium hydroxide (NaOH), were purchased from Aladdin Biochemical Technology Co., Ltd. (Shanghai, China).

Preparation of PANI/SL and PANI@SL

First, 0.3 g of SL was dissolved in deionized water in a 50 mL round-bottom flask. Then, 0.3 g of ANI monomer was added dropwise, and the mixture was ultrasonicated for 30 min to achieve homogeneous dispersion. Separately, 1.2 g of APS was dissolved in deionized water and pre-cooled in a refrigerator. The APS solution was then added dropwise to the ANI/SL mixture under continuous magnetic stirring in an ice-water bath. The reaction was allowed to proceed under magnetic stirring in the ice-water bath for 1 h, followed by standing at room temperature for 12 h to complete the polymerization. The resulting product was collected by centrifugation, and the supernatant was discarded. The solid was thoroughly washed with deionized water via repeated centrifugation cycles until the supernatant reached neutral pH, ensuring the removal of residual reactants and by-products. Finally, the product was dried in an air-drying oven at 80 °C to obtain the PANI/SL composite. For comparison, a physically mixed control sample, designated PANI@SL, was prepared by thoroughly ball-milling commercially available SL with intrinsic PANI at a 1:1 mass ratio.

Characterization

The morphology and microstructure of the samples were characterized by scanning electron microscopy (SEM, Zeiss Merlin) and transmission electron microscopy (TEM, Thermo Fisher Scientific Talos F200X G2). The specific surface area and pore structure were determined from N_2 adsorption-desorption isotherms measured at 77 K using a

Micromeritics ASAP 2460 analyzer. Chemical structures were analyzed by Raman spectroscopy (Horiba LabRAM HR Evolution, 532 nm laser) and Fourier transform infrared (FTIR) spectroscopy (NICOLET iS50). Thermal stability was assessed via thermogravimetric (TG, NETZSCH TG209F3) analysis. The X-ray diffraction (XRD) measurements were performed using a Bruker D8 ADVANCE diffractometer (Bruker, Germany). The optical properties were evaluated using a Shimadzu UV-3600 UV-Vis spectrophotometer. The electronic structure was probed by X-ray photoelectron spectroscopy (XPS, Thermo Scientific K-Alpha Nexsa) and electron paramagnetic resonance (EPR) spectroscopy (Bruker ELEXSYS E500).

Electrochemical measurements, including galvanostatic charge-discharge (for rate and cycling performance) and galvanostatic intermittent titration technique (GITT), were performed on a LAND CT2001A battery test system. Cyclic voltammetry (CV) and *in situ* electrochemical impedance spectroscopy (EIS) were conducted using a CHI 760E electrochemical workstation. *In situ* Raman spectroscopy measurements were carried out on a Horiba LabRAM HR Evolution spectrometer coupled with the CHI 760E workstation.

DFT Calculations

Density Functional Theory (DFT) computations were carried out with Gaussian 16.[1] Geometry optimizations were performed using the B3LYP functional in conjunction with the 6-31G(d,p) basis set.[2] The convergence thresholds for geometry optimizations adopted the default tight criteria of Gaussian 16. SCF convergence was deemed achieved when the energy difference between consecutive cycles fell below 1×10^{-6} Hartree and the variation in the density matrix was less than 1×10^{-8}. All calculations utilized an ultrafine integration grid (Int=UltraFine) and tight SCF convergence criteria (SCF=Tight). For systems exhibiting convergence challenges, the quadratic convergence algorithm (SCF=XQC) was implemented to ensure robust SCF convergence. Non-covalent interaction analysis was executed using Multiwfn via reduced density gradient (RDG) calculations, facilitating the identification of distinct

non-covalent interaction regions within the PANI/SL composite system. The adsorption energy (E_{ads}) is calculated as follows. $E_{ads} = E_{tot}-E_{slab}-E_X$. E_{tot} and E_{slab} are the energy of the base adsorbed Na, and the energy of the substrate, respectively, and E_X is the energy of the Na.

Electrochemical Measurements

The working electrode was prepared by homogeneously mixing the active material, Super-P carbon conductive additive, and sodium carboxymethyl cellulose (CMC) binder at a mass ratio of 7:2:1 in deionized water, followed by magnetic stirring to form a homogeneous slurry. The resulting slurry was then cast onto a copper foil current collector and vacuum-dried at 100 °C for 12 h. The dried electrode film was punched into 12-mm-diameter discs with an active material mass loading of 0.8-1.2 mg cm^{-2}.

The $Na_3V_2(PO_4)_3$ (NVP) cathode was fabricated by mixing NVP powder, Super P carbon black, and polyvinylidene fluoride (PVDF) binder in a weight ratio of 8:1:1. The mixture was dispersed in N-methyl-2-pyrrolidone (NMP) solvent and stirred thoroughly to form a homogeneous slurry. The resulting slurry was then coated onto an aluminum foil current collector using a doctor blade coating method. The coated electrode was dried under vacuum at 100 °C for 12 h to completely remove the solvent. Subsequently, the dried electrode was punched into circular discs with a diameter of 12 mm. The mass loading of the active material was approximately 2 mg cm^{-2}.

All reported current densities and capacities are normalized to the mass of the active material. CR2032-type coin cells were assembled in an argon-filled glove box, where the concentrations of O_2 and H_2O were rigorously controlled below 0.1 ppm. The cell configuration consisted of the prepared working electrode, a sodium metal counter/reference electrode (14 mm in diameter), a glass fiber (GF/D) separator (16 mm in diameter), and 1 M sodium hexafluorophosphate ($NaPF_6$) dissolved in dimethoxyethane (DME) as the electrolyte. All electrochemical measurements were

performed at 25 °C.

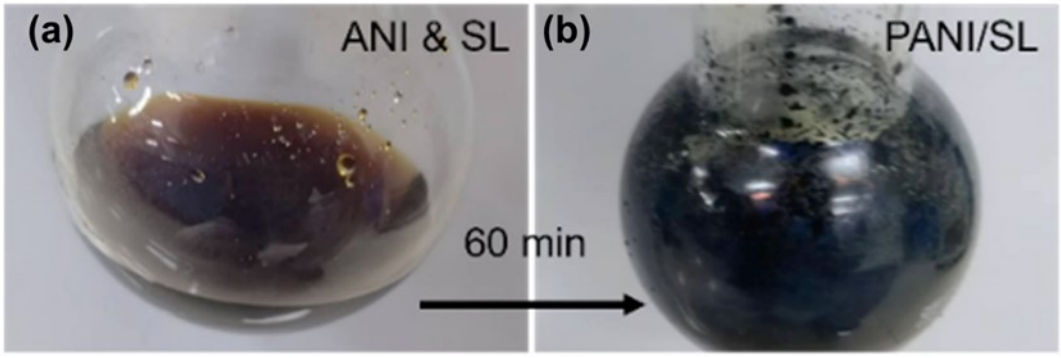

Fig. S1. Digital photographs of the samples: the in-situ polymerization reaction (a) before and (b) after the reaction.

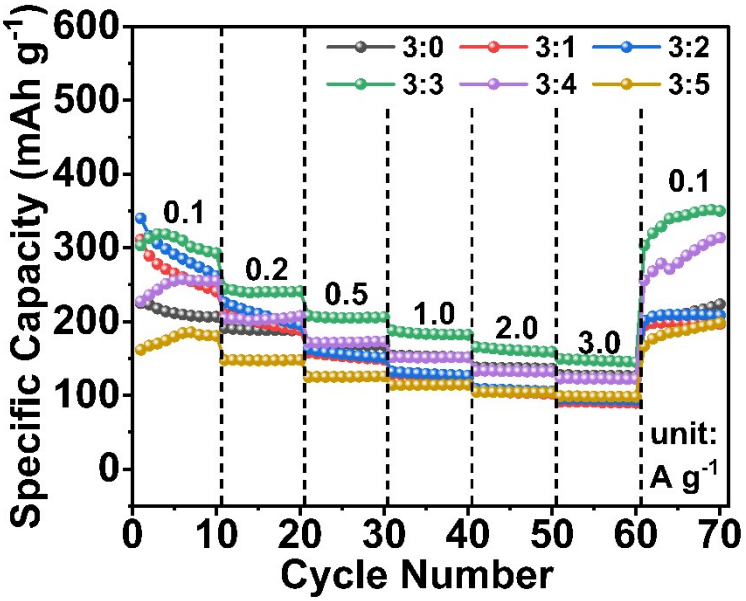

Fig. S2. Effect of ANI/SL mass ratio on the rate performance of the resulting composite anode materials.

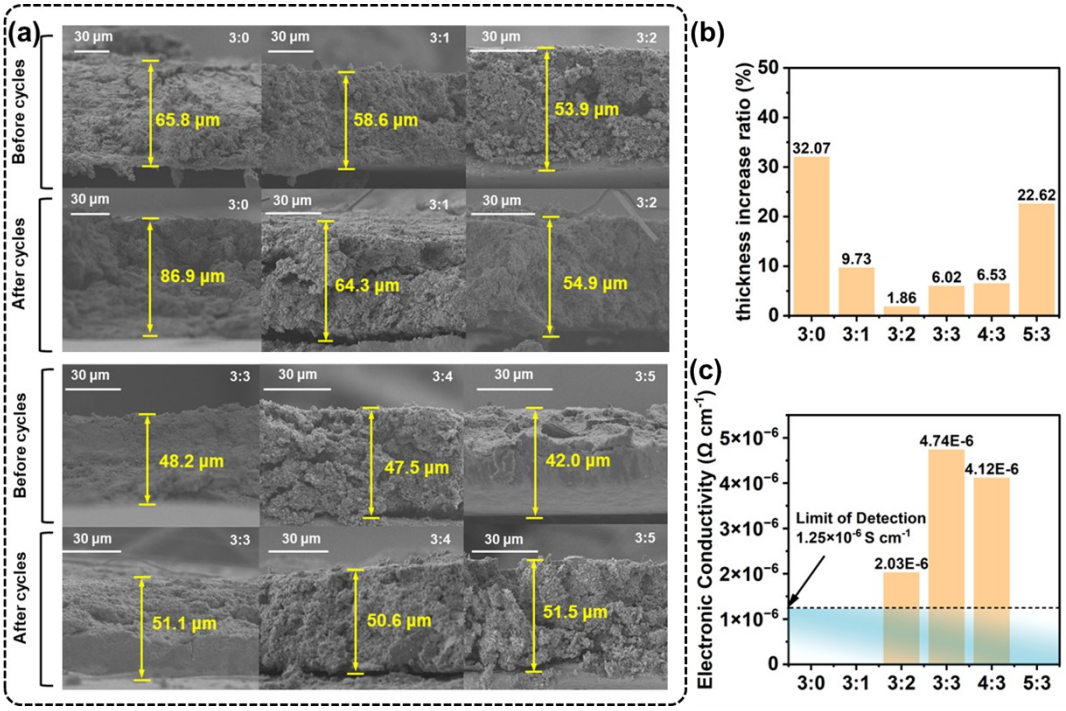

Fig. S3 Effect of ANI/SL mass ratio on (a) the SEM images of volume expansion (before and after 2000 cycles at a current density of 2.0 A g^{-1} , with a mass loading of ~1 mg cm^{-2}), (b) electrode thickness increase ratio, and (c) electrical conductivity of the composites. The electrical conductivity was measured using pellets pressed at 20 MPa.

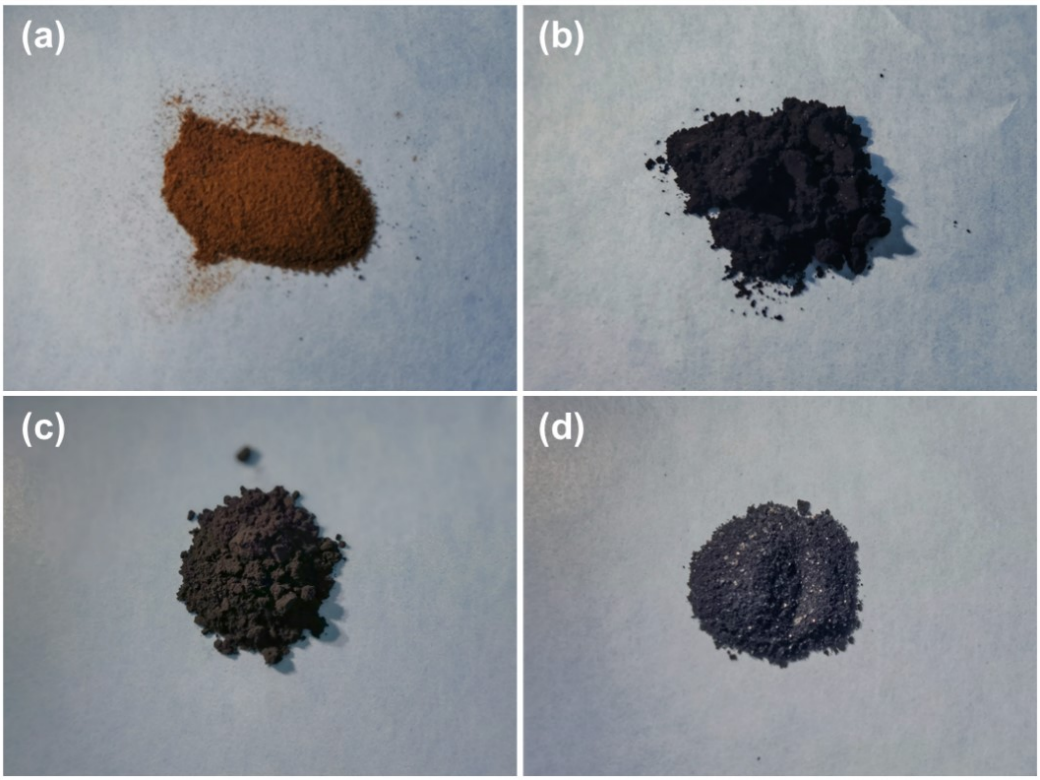

Fig. S4. Photographs of four OEMs: (a) SL, (b) PANI, (c) PANI@SL, and (d) PANI/SL.

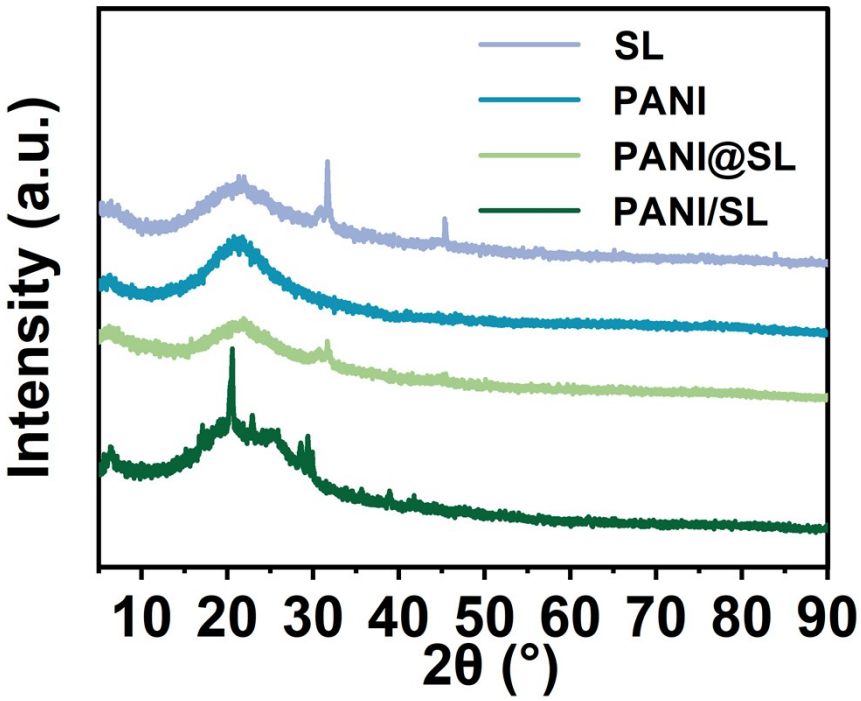

Fig. S5. XRD patterns of four OEMs: SL, PANI, PANI@SL and PANI/SL.

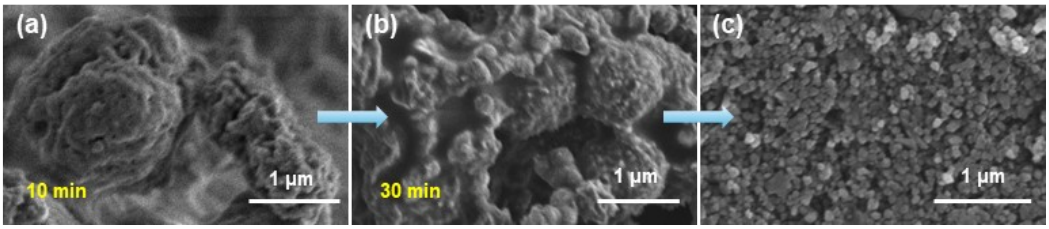

Fig. S6. SEM images showing the morphological evolution of the PANI/SL composite during *In situ* polymerization after (a) 10 min, (b) 30 min, and (c) 60 min (the final product).

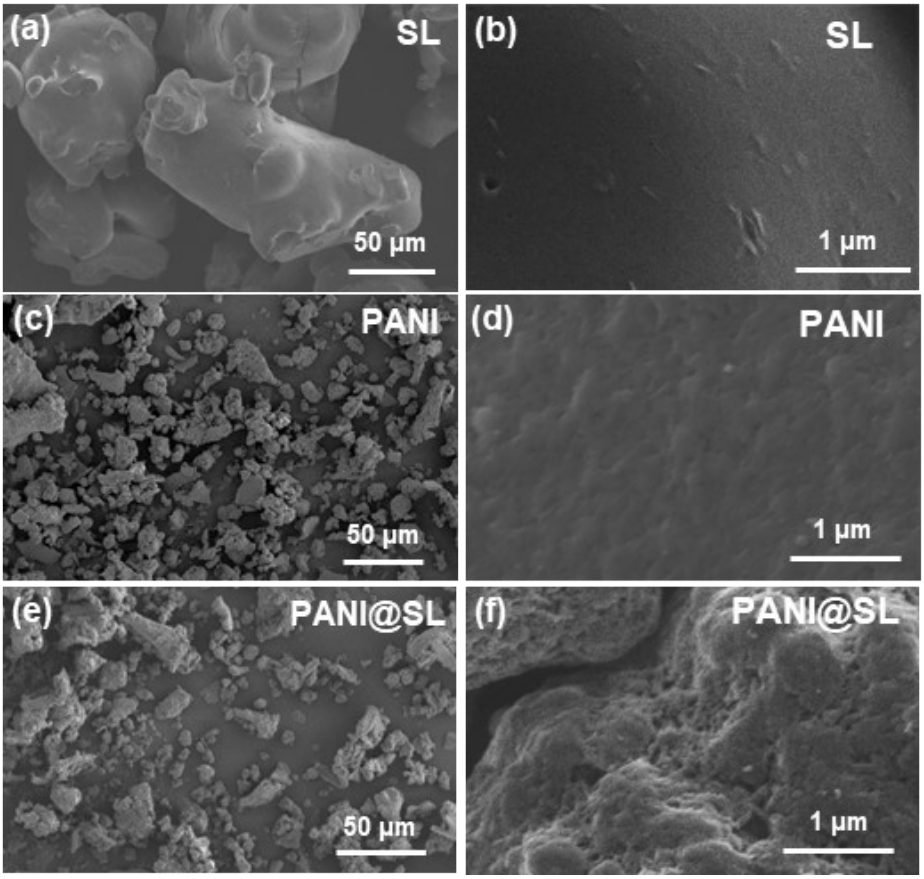

Fig. S7. Representative SEM images at different magnifications of (a, b) SL, (c, d) PANI, and (e, f) PANI@SL.

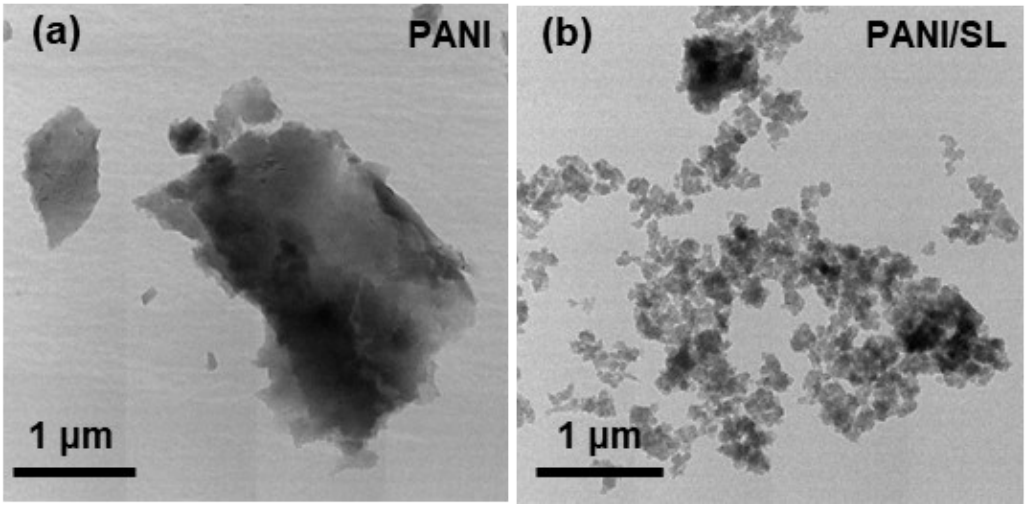

Fig. S8. TEM images of (a) PANI and (b) PANI/SL.

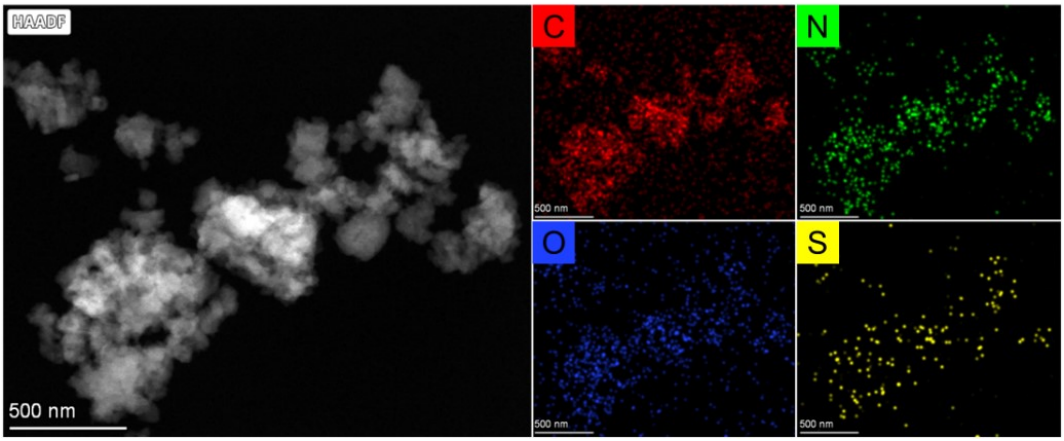

Fig. S9. TEM elemental mapping of PANI/SL.

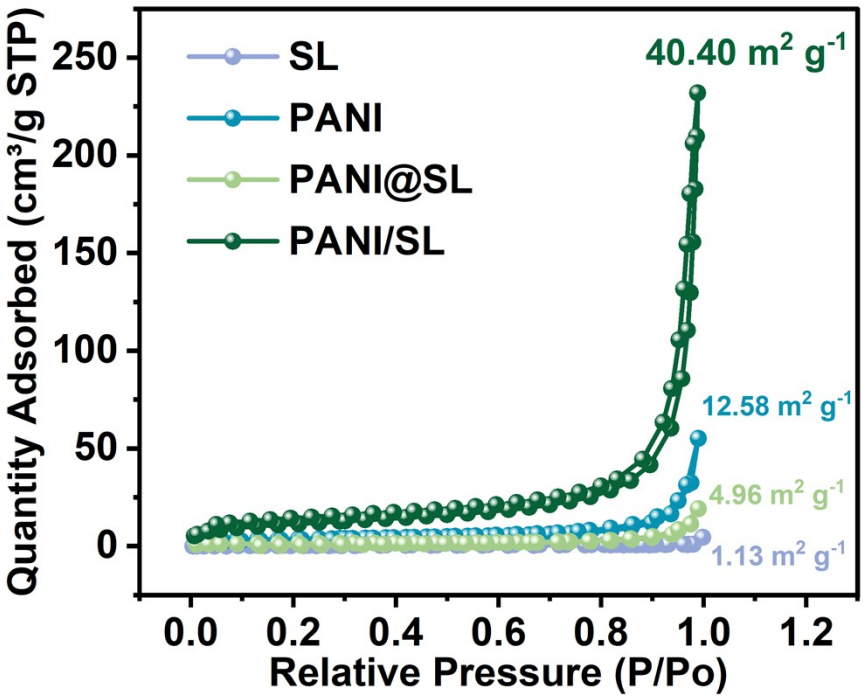

Fig. S10. N_2 adsorption-desorption isotherms and the corresponding specific surface area of four OEMs: SL, PANI, PANI@SL and PANI/SL.

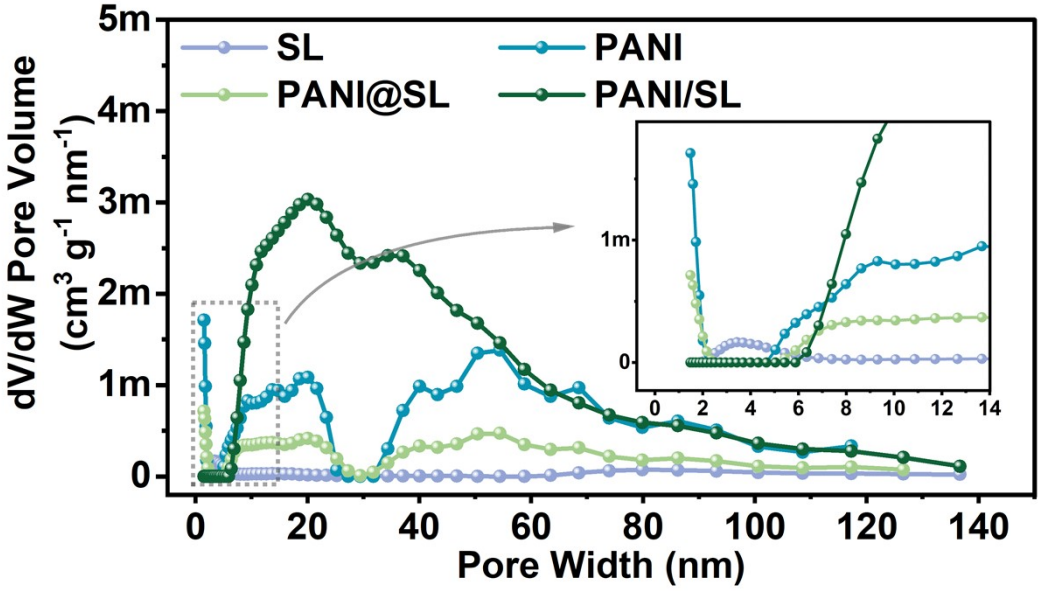

Fig. S11. Pore size distribution derived from DFT calculations of four OEMs: SL, PANI, PANI@SL and PANI/SL.

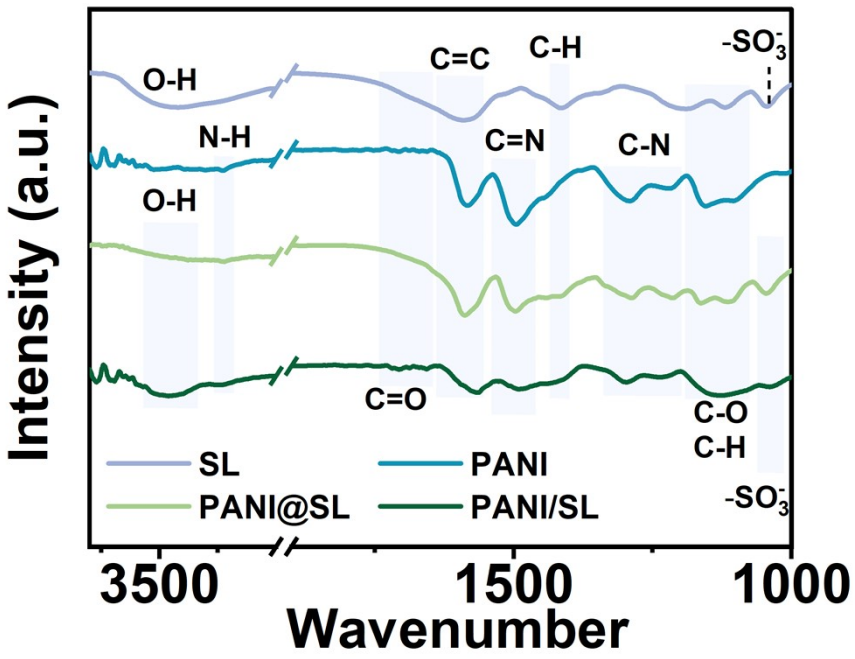

Fig. S12. FTIR spectra of four OEMs: SL, PANI, PANI@SL and PANI/SL.

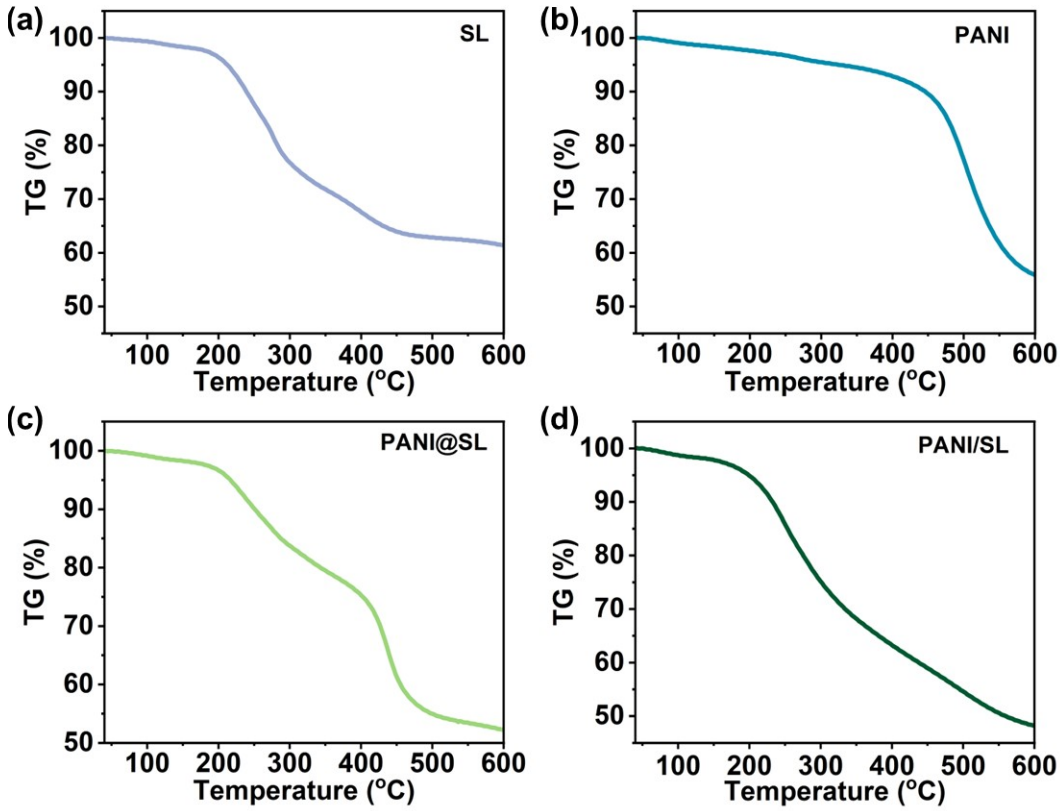

Fig. S13. TGA curves of four OEMs: (a) SL, (b) PANI, (c) PANI@SL and (d) PANI/SL.

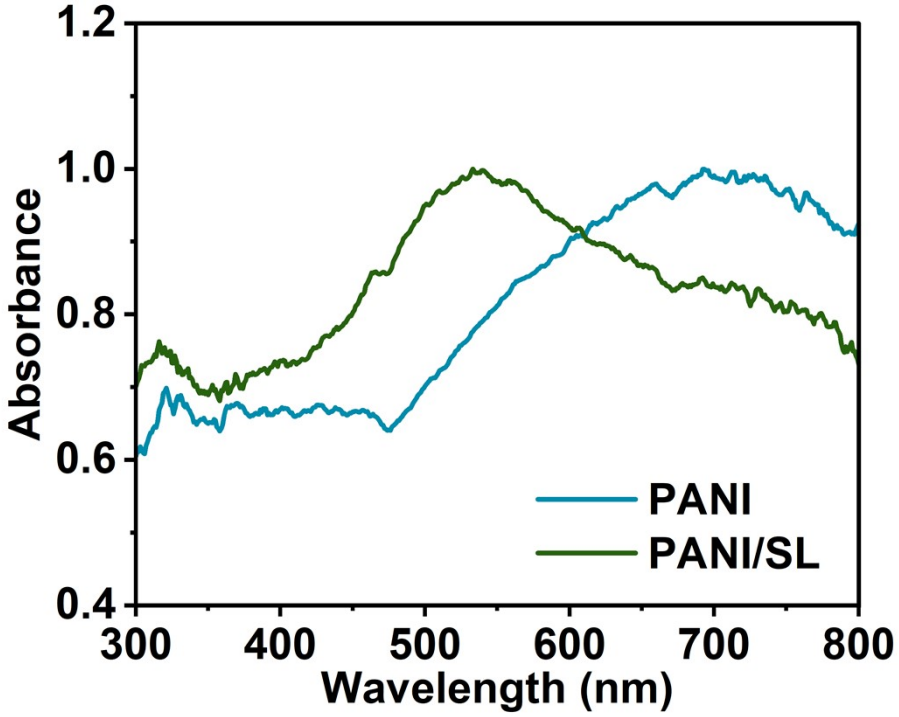

Fig. S14 Comparison of solid-state UV-Vis spectra.

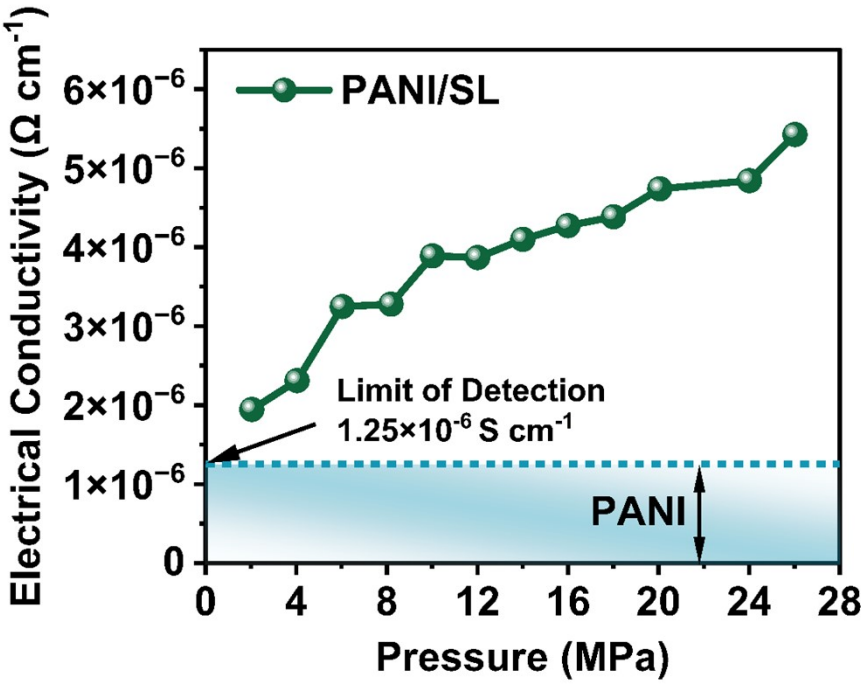

Fig. S15. Electronic conductivity of the PANI/SL composite plotted against the compaction pressure.

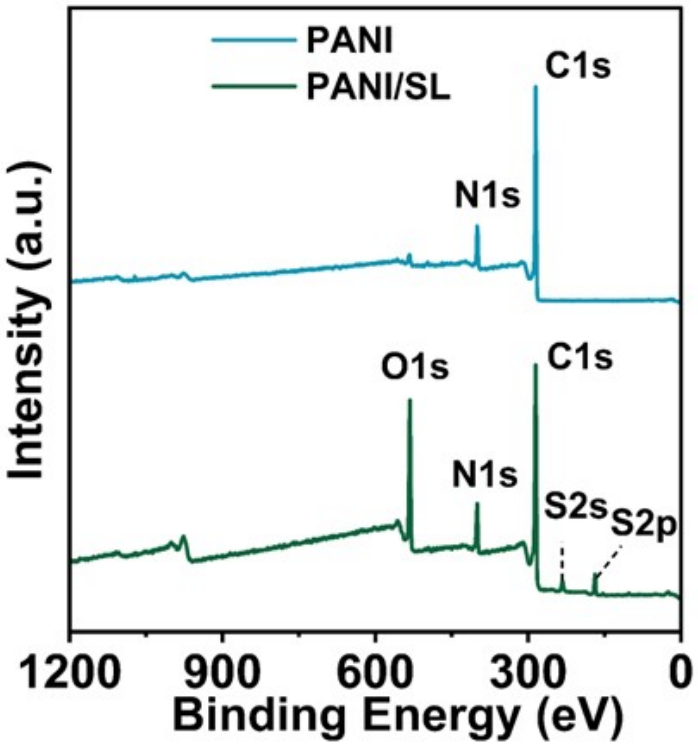

Fig. S16. XPS spectra of PANI and PANI/SL.

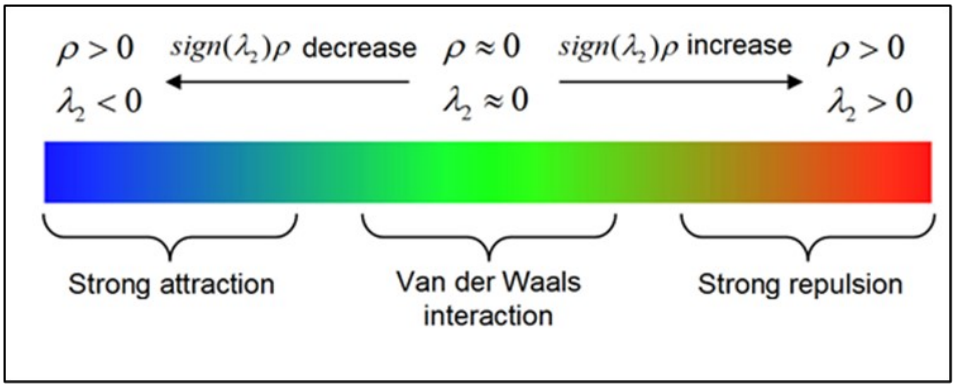

Fig. S17. RDG Isosurface Diagram.

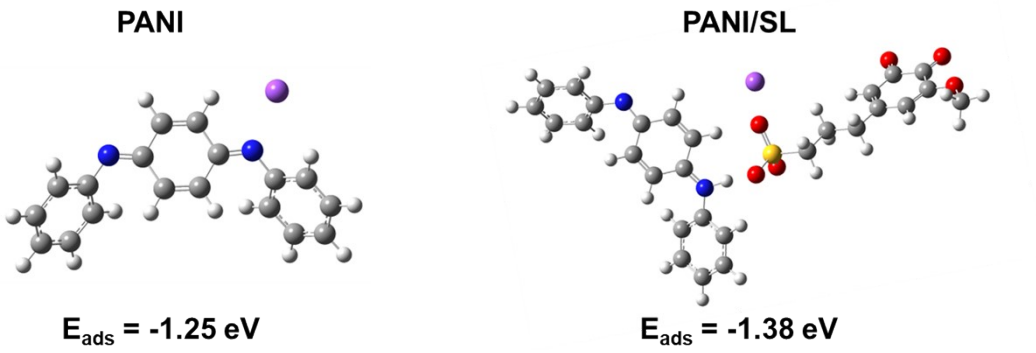

Fig. S18 Na^+ adsorption energies of PANI and PANI/SL.

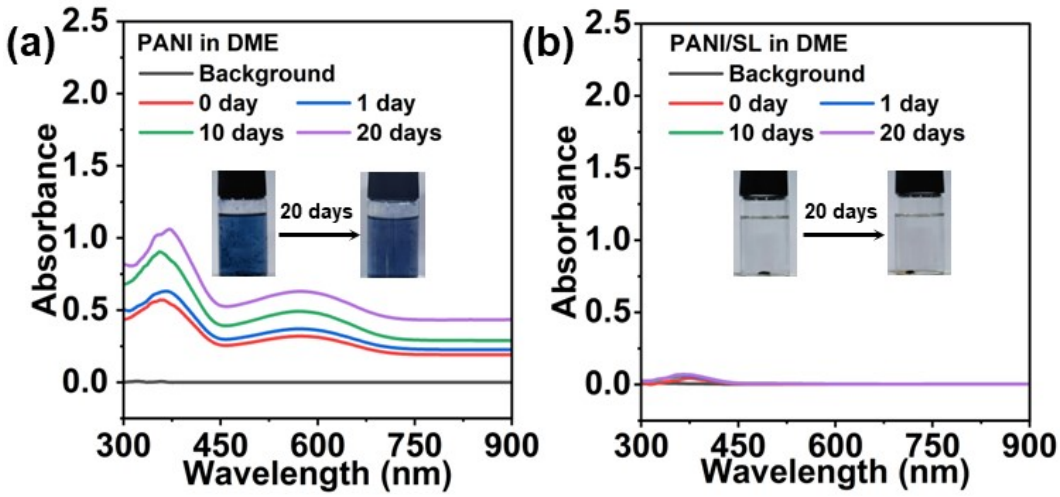

Fig. S19. Temporal evolution of UV-Vis spectra for (a) PANI and (b) PANI/SL immersed in DME over different numbers of days

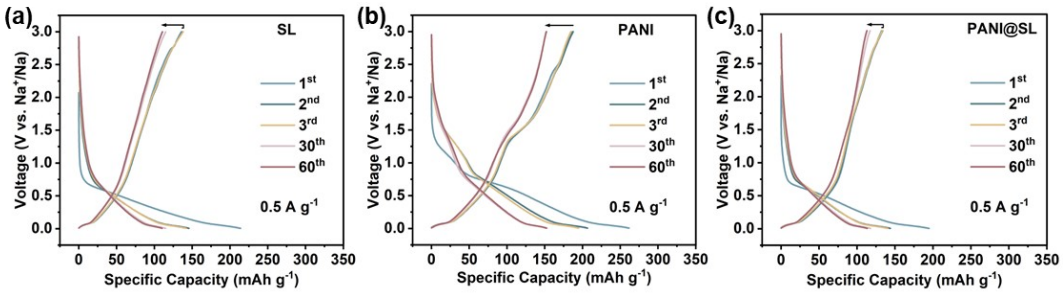

Fig. S20. GCD curves of (a) SL, (b) PANI, and (c) PANI@SL at 0.5 A g^{-1}.

Table S1. Comparison of the cycling performance of different organic anode materials for SIBs.

Anode Material	Cycle number	Current density (A g^{-1})	Capacity retention rate (%)	Ref.
Cu-TBP	800	0.25	82.6	[3]
Lignin	200	1	91.9	[4]
PTCDA	1000	2	94	[5]
BMHCS	300	1	90	[6]
Cabpdc/rGO	100	0.1	90.7	[7]
TBC	600	0.05	70.24	[8]
TQA	100	0.35	85	[9]
Fe-CPNWs/rGO	2000/4000	0.5/1	40/20	[10]
O-*p*NaPc	200	0.2	95.8	[11]
HATN-SCu	1000	2	56.3	[12]
PANI/SL	**3800**	**2**	**99.2**	**This work**

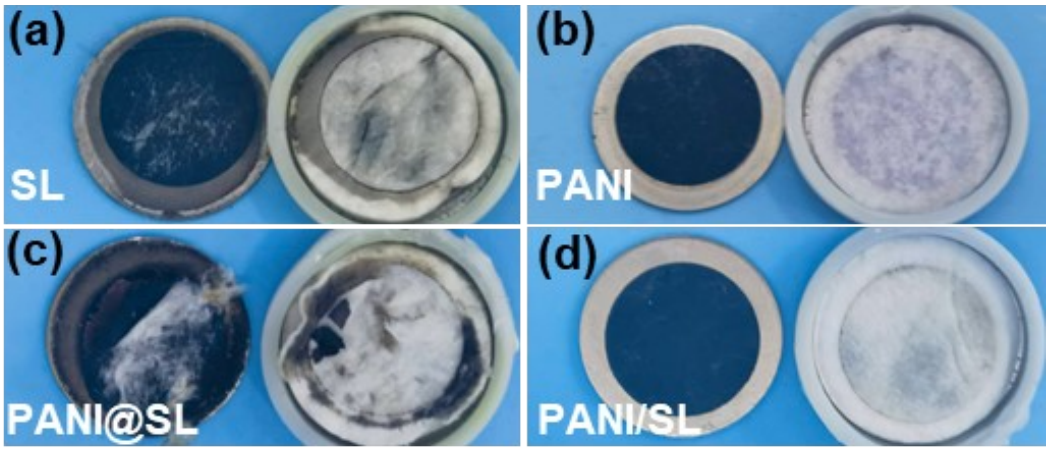

Fig. S21. Photographs of the electrodes and separators from disassembled half-cells of (a) SL, (b) PANI, (c) PANI@SL, and (d) PANI/SL after cycles.

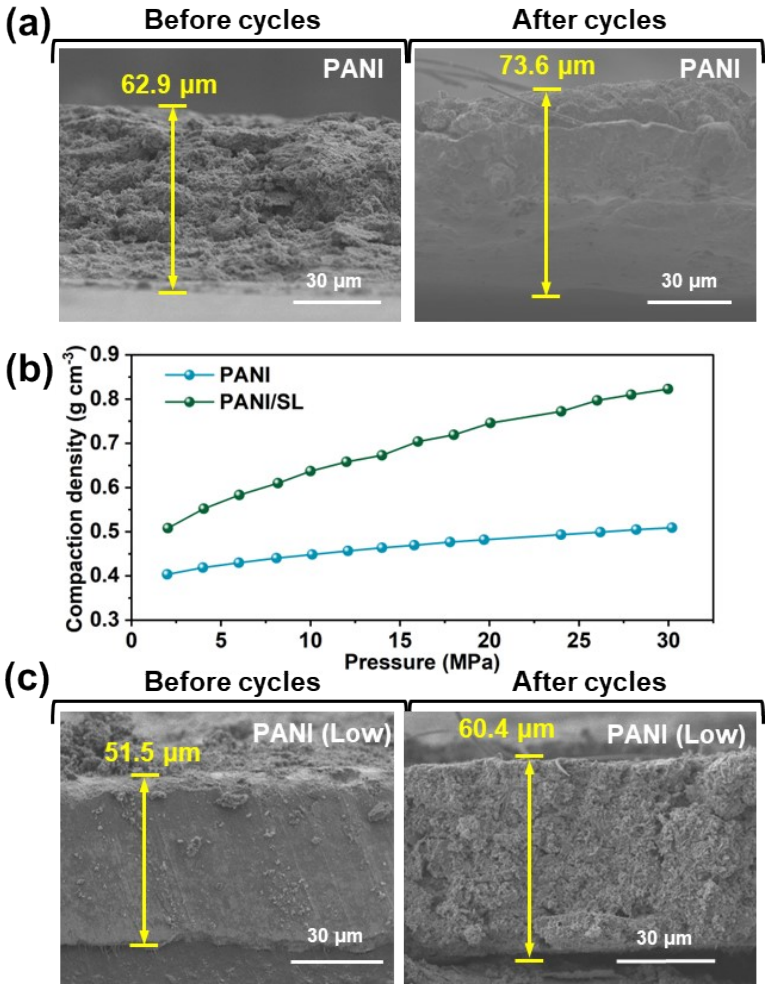

Fig. S22. (a) SEM cross-sectional images of the PANI electrodes with a mass loading of ~1 mg cm^{-2} before and after 2000 cycles at a current density of 2.0 A g^{-1}. (b) Comparison of the compaction density between PANI and PANI/SL. (c) SEM cross-sectional images of the PANI electrodes (prepared with a low mass loading of ~0.8 mg cm^{-2} to ensure consistent thickness with PANI/SL) before and after 2000 cycles at a current density of 2.0 A g^{-1}.

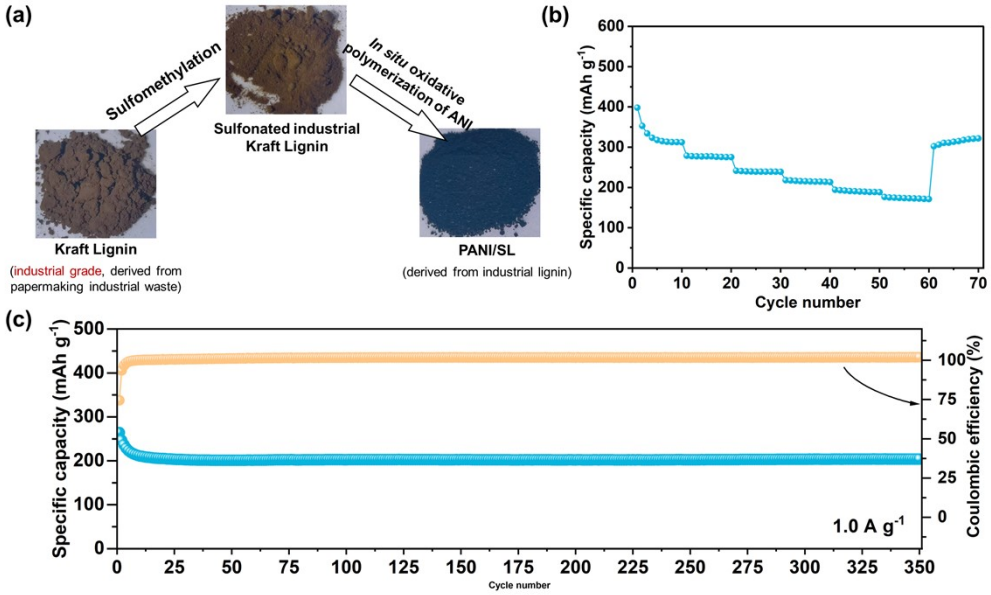

Fig. S23 (a) Digital photographs of industrial Kraft lignin, sulfonated industrial Kraft lignin, and PANI/SL (derived from industrial lignin). (b) Rate capability and (c) cycling stability of the PANI/SL (derived from industrial lignin) anode.

Preparation of sulfonated industrial Kraft lignin: Kraft lignin was first dissolved in 1 M NaOH solution to form a homogeneous alkaline solution. Then, 37 wt% formaldehyde solution (1.2 g per 10 g lignin) was added dropwise, and the mixture was stirred at 60 °C for 1 h to achieve hydroxymethyl activation. After that, Na_2SO_3 (1.5 g per 10 g lignin) was introduced, and the reaction was continued at 95 °C for 3 h under vigorous stirring. After cooling to room temperature, the solution was neutralized, dialyzed to remove small-molecule impurities, and freeze-dried to obtain sulfonated industrial Kraft lignin.

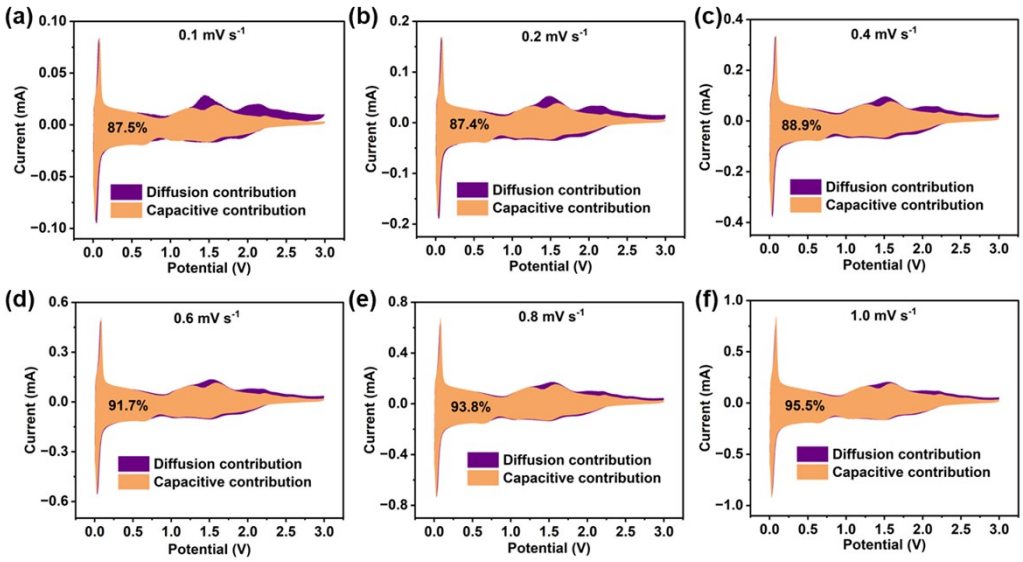

Fig. S24. Capacitive contribution (orange region) of PANI at a scan rate of (a) 0.1, (b) 0.2, (c) 0.4, (d) 0.6, (e) 0.8 and (f) 1.0 mV s^{-1}.

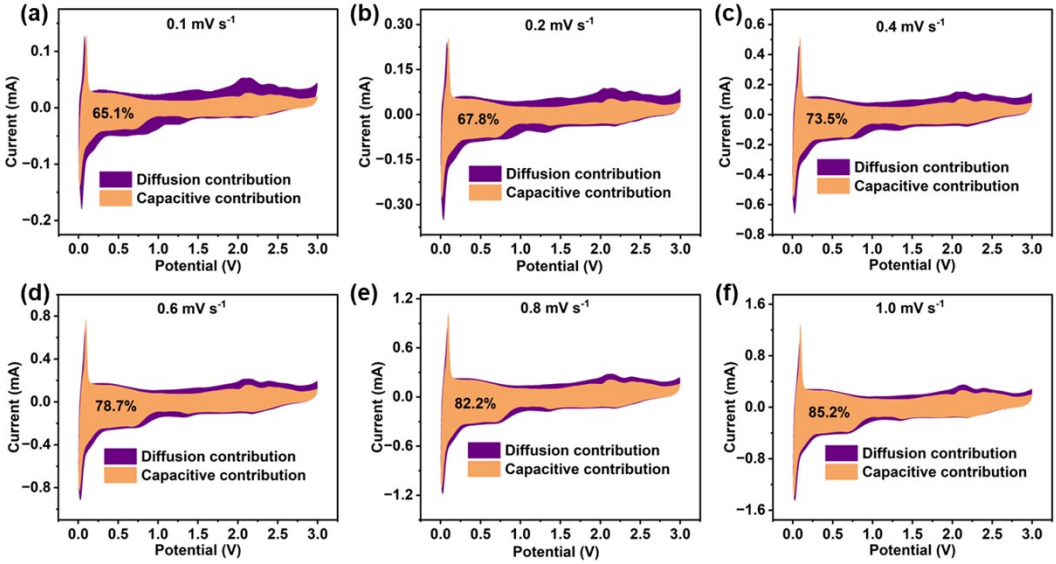

Fig. S25. Capacitive contribution (orange region) of PANI/SL at a scan rate of (a) 0.1, (b) 0.2, (c) 0.4, (d) 0.6, (e) 0.8 and (f) 1.0 mV s^{-1}.

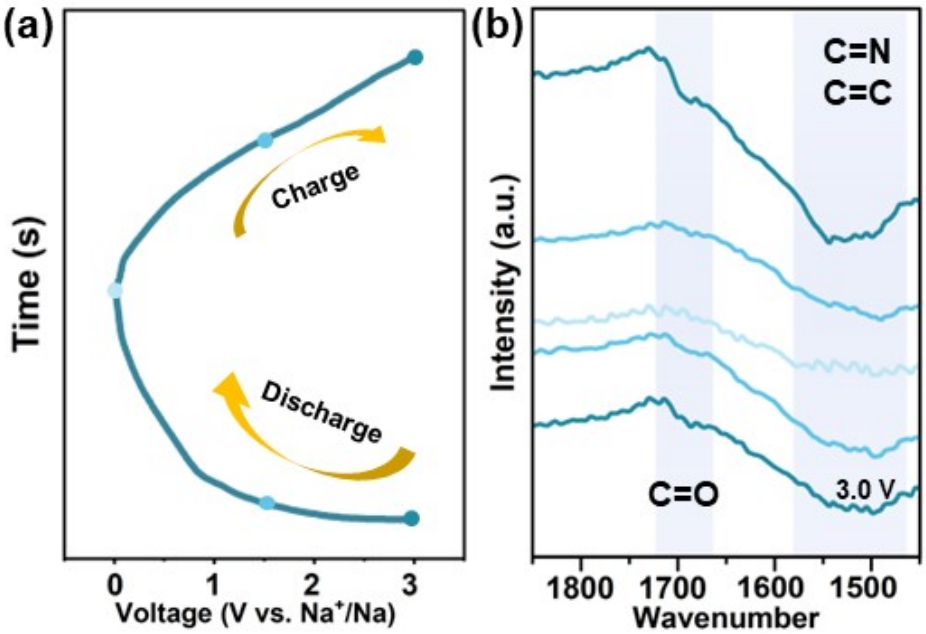

Fig. S26. (a) GCD profile of PANI/SL and the corresponding (b) *ex situ* FTIR spectra (after 5 pre-cycles at 0.2 A g^{-1}).

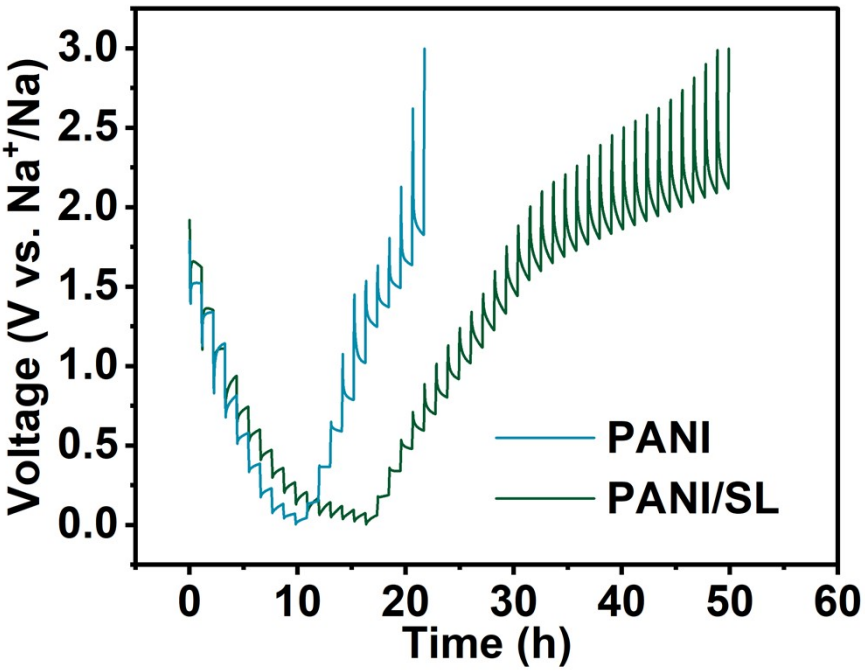

Fig. S27. Voltage–time profiles of PANI and PANI/SL during the GITT measurement.

References

1. M. Frisch et al., Gaussian 16 Rev. A.03, Wallingford, CT, 2016.
2. A. Becke, *J. Chem. Phys.*, 1992, **96**, 2155–2160.
3. J. Yin, X. Lian, J. Zhang, Z. Li, M. Liu, J. Pang, W. Li, Y. Xu, N. Li and X. Bu, *Angew. Chem. Int. Ed.*, 2025, **64**, e202510698.
4. Y. She, X. Li, Y. Zheng, D. Chen, X. Rui, X. Lin and Y. Qin, *Energy Environ. Mater.*, 2024, **7**, e12538.
5. H. Wu, T. Hu, S. Chang, L. Li and W. Yuan, *ACS Appl. Mater. Interfaces*, 2021, **13**, 44254–44265.
6. H. Yang, A. Li, C. Zhou, X. Liu, X. Chen, H. Liu, T. Liu and H. Song, *Nanomaterials*, 2022, **12**, 3926.
7. T. Aro and P. Fatehi, *ChemSusChem*, 2017, **10**, 1861–1877.
8. C. Luo, J. Shea and J. Huang, *J. Power Sources*, 2020, **453**, 227904.
9. Q. Zhao, W. Zhao, C. Zhang, Y. Wu, Q. Yuan, A. Whittaker and X. Zhao, *Energy Fuels*, 2020, **34**, 5099–5105.
10. Z. Sun, K. Tan, L. Hou, Y. Liu and C. Yuan, *Sci. China Mater.*, 2020, **63**, 1966–1972.
11. J. Lee, Y. Kim, S. Park, K. Shin, G. Jang, M. Hwang, D. Kim, K. Min, H. Park, B. Han, D. Ng and L. Lee, *Energy Environ. Mater.*, 2023, **6**, e12468.
12. B. Wang, J. Li, M. Ye, Y. Zhang, Y. Tang, X. Hu, J. He and C. Li, *Adv. Funct. Mater.*, 2022, **32**, 2112072.